

---

This is an electronic reprint of the original article.  
This reprint may differ from the original in pagination and typographic detail.

Ngo, Tien Dat; Huynh, Tuyen; Jung, Hanggyo; Ali, Fida; Jeon, Jongwook; Choi, Min Sup;  
Yoo, Won Jong

## Modulation of Contact Resistance of Dual-Gated MoS<sub>2</sub> FETs Using Fermi-Level Pinning-Free Antimony Semi-Metal Contacts

*Published in:*  
Advanced Science

*DOI:*  
[10.1002/adv.202301400](https://doi.org/10.1002/adv.202301400)

Published: 27/07/2023

*Document Version*  
Publisher's PDF, also known as Version of record

*Published under the following license:*  
CC BY

*Please cite the original version:*  
Ngo, T. D., Huynh, T., Jung, H., Ali, F., Jeon, J., Choi, M. S., & Yoo, W. J. (2023). Modulation of Contact Resistance of Dual-Gated MoS<sub>2</sub> FETs Using Fermi-Level Pinning-Free Antimony Semi-Metal Contacts. *Advanced Science*, 10(21), Article 2301400. <https://doi.org/10.1002/adv.202301400>

---

This material is protected by copyright and other intellectual property rights, and duplication or sale of all or part of any of the repository collections is not permitted, except that material may be duplicated by you for your research use or educational purposes in electronic or print form. You must obtain permission for any other use. Electronic or print copies may not be offered, whether for sale or otherwise to anyone who is not an authorised user.

# Modulation of Contact Resistance of Dual-Gated MoS<sub>2</sub> FETs Using Fermi-Level Pinning-Free Antimony Semi-Metal Contacts

Tien Dat Ngo, Tuyen Huynh, Hanggyo Jung, Fida Ali, Jongwook Jeon, Min Sup Choi,\* and Won Jong Yoo\*

Achieving low contact resistance ( $R_C$ ) is one of the major challenges in producing 2D FETs for future CMOS technology applications. In this work, the electrical characteristics for semimetal (Sb) and normal metal (Ti) contacted MoS<sub>2</sub> devices are systematically analyzed as a function of top and bottom gate-voltages ( $V_{TG}$  and  $V_{BG}$ ). The semimetal contacts not only significantly reduce  $R_C$  but also induce a strong dependence of  $R_C$  on  $V_{TG}$ , in sharp contrast to Ti contacts that only modulate  $R_C$  by varying  $V_{BG}$ . The anomalous behavior is attributed to the strongly modulated pseudo-junction resistance ( $R_{jun}$ ) by  $V_{TG}$ , resulting from weak Fermi level pinning (FLP) of Sb contacts. In contrast, the resistances under both metallic contacts remain unchanged by  $V_{TG}$  as metal screens the electric field from the applied  $V_{TG}$ . Technology computer aided design simulations further confirm the contribution of  $V_{TG}$  to  $R_{jun}$ , which improves overall  $R_C$  of Sb-contacted MoS<sub>2</sub> devices. Consequently, the Sb contact has a distinctive merit in dual-gated (DG) device structure, as it greatly reduces  $R_C$  and enables effective gate control by both  $V_{BG}$  and  $V_{TG}$ . The results offer new insight into the development of DG 2D FETs with enhanced contact properties realized by using semimetals.

## 1. Introduction

Transition-metal dichalcogenides (TMDs) are a promising candidate for semiconducting channel materials that are expected to be useful in future CMOS devices due to their bodies that are atomically thin and free of dangling bonds, thus enabling efficient electrostatic control at very low voltages. One of the most studied materials among this TMD family is MoS<sub>2</sub>. In recent years, there have been many efforts aiming to further improve the performance of 2D-based FETs, e.g., contact engineering.<sup>[1–7]</sup> However, the notoriously high contact resistance ( $R_C$ ) in MoS<sub>2</sub> FETs hinders the realization of high-performance electronic devices. Several techniques have recently been reported to improve  $R_C$  by utilizing semimetals as contact metals for MoS<sub>2</sub> FETs, which can substantially suppress the metal-induced gap states (MIGS).<sup>[8–15]</sup>

Nonetheless, most studies have investigated the contact properties in a single-gated (SG) architecture rather than a dual-gated (DG) architecture. Conventional SG planar devices encounter a severe challenge such as poor electrostatic controllability due to their short channel effects, which hinders further scaling of the devices. By contrast, the DG can enable more efficient control of the channel resistance of 2D layered material-based FET devices, and it can also be used for high-performance and variously designed gate-integrated CMOS circuits.<sup>[16–20]</sup> Several studies have used multi-bridge channel FETs, which are analogous to a DG structure, to achieve excellent electrostatic controllability and power/area efficiency.<sup>[21–24]</sup> Moreover, a research group has recently explored DG MoS<sub>2</sub> FETs with a channel length of 25 nm, which show a comparable performance to state-of-the-art Si technology.<sup>[25]</sup> Thus, the DG architectures of high-performance 2D FETs need to be developed to ensure a long-term continuity of Moore's Law scaling.


Meanwhile, some studies have shown that overall  $R_C$  is independent of top-gate voltage ( $V_{TG}$ ) in DG FETs, because the  $V_{TG}$ -induced electric field can be screened by metal electrodes, resulting in unchanged intrinsic resistance under the contacts ( $R_{ci}$ ).<sup>[19,20]</sup> It should be noted that the normal metals used in these studies induce strong Fermi level pinning (FLP) at the

T. D. Ngo, T. Huynh, W. J. Yoo  
SKKU Advanced Institute of Nano Technology  
Sungkyunkwan University  
Suwon, Gyeonggi-do 16419, Republic of Korea  
E-mail: yoowj@skku.edu

H. Jung, J. Jeon  
Department of Electrical and Electronics Engineering  
Konkuk University  
Seoul 05029, Republic of Korea

F. Ali  
Department of Electronics and Nanoengineering  
Aalto University  
P.O. Box 13500, Espoo FI-00076, Finland

M. S. Choi  
Department of Materials Science and Engineering  
Chungnam National University  
Daejeon 34134, Republic of Korea  
E-mail: goodcms@cnu.ac.kr

 The ORCID identification number(s) for the author(s) of this article can be found under <https://doi.org/10.1002/advs.202301400>

© 2023 The Authors. Advanced Science published by Wiley-VCH GmbH. This is an open access article under the terms of the Creative Commons Attribution License, which permits use, distribution and reproduction in any medium, provided the original work is properly cited.

DOI: 10.1002/advs.202301400

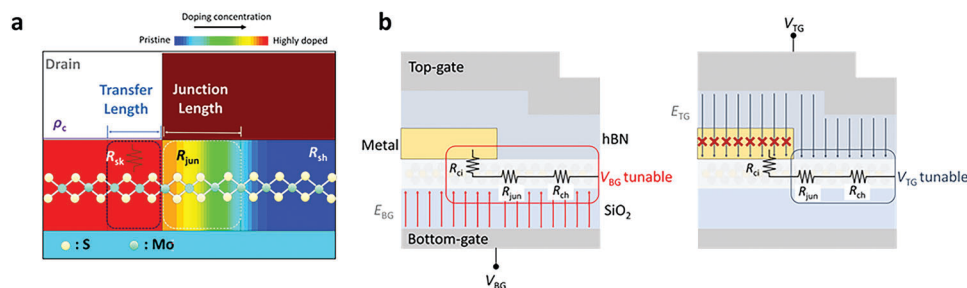


**Figure 1.** a) Schematic of a MoS<sub>2</sub> FET at the drain contact side showing doping concentration profile at the contact and channel regions. b) Schematic of a DG MoS<sub>2</sub> FET showing  $R_C$  components that consist of  $R_{ci}$  and  $R_{junn}$ . The  $E_{TG}$  is screened by the metal electrode, while the  $E_{BG}$  can tune all the  $R_C$  components.

metal–semiconductor (MS) interface; therefore, the lateral junction resistances near the contacts are also unchanged by  $V_{TG}$ .<sup>[26–28]</sup> Recently, to reveal such FLP-dependent contact behaviors, the classical model on contact interface between metal and semiconductor involving specific contact resistivity ( $\rho_c$ ) and sheet resistance under the metal contact ( $R_{sk}$ ) has been further developed by adding pseudo-lateral junction resistance ( $R_{junn}$ ) components to the total  $R_C$  in 2D-based FETs.<sup>[29–31]</sup> Venica et al. first proposed the use of the  $R_{junn}$  component to explain the gate-tunable  $R_C$ .<sup>[30]</sup> Moreover, Ber et al. proposed a unique approach to specifically probe the  $R_{junn}$  component by 4-point probe (4PP) measurements, which also helps to extract various metallic contact-related resistance components.<sup>[29]</sup> Meanwhile, Kong et al. performed a DFT band calculation that showed clear differences in the contact resistance components between FLP-dominant and FLP-free metal contact platforms.<sup>[32]</sup>

In this work, we used a semimetal (antimony, Sb) as a top surface electrode and hBN as a top-gate (TG) dielectric for the purpose of realizing an FLP-free MS interface in DG MoS<sub>2</sub> FETs. Ohmic contact is realized with the Sb contact by suppressing MIGS at the Sb and MoS<sub>2</sub> interface.<sup>[8,9]</sup> We performed systematic 4PP measurements to extract  $R_C$  as a function of bottom-gate voltage ( $V_{BG}$ ) and  $V_{TG}$ . Interestingly, our Sb-contacted devices showed that  $R_C$  is modulated sensitively by both  $V_{TG}$  and  $V_{BG}$ , which is in sharp contrast with Ti-contacted devices showing  $R_C$  modulation only by  $V_{BG}$ . To further understand this anomalous contact behavior of Sb-contacted devices, we extracted  $R_{junn}$  and  $R_{ci}$  as functions of DG voltages.<sup>[29]</sup> The results showed that  $R_{junn}$  is significantly modulated by both  $V_{TG}$  and  $V_{BG}$  while  $R_{ci}$  is modulated only by  $V_{BG}$ . By contrast,  $R_{junn}$  and  $R_{ci}$  of Ti-contacted devices are weakly tuned by  $V_{TG}$  due to strong FLP. This work suggests that the FLP-free semimetal contacts can be used to efficiently modulate  $R_C$  in DG MoS<sub>2</sub> FETs by applying both  $V_{BG}$  and  $V_{TG}$ . Technology computer-aided design (TCAD) simulations further confirm the role of  $V_{TG}$  in improving  $R_{junn}$  toward high-performance Sb-contacted DG MoS<sub>2</sub> devices.

## 2. Results and Discussion

**Figure 1a** shows a schematic of MoS<sub>2</sub> FET with  $R_C$  components at the MS contact. To systematically investigate the impacts of  $V_{BG}$  and  $V_{TG}$  on overall  $R_C$ , we decompose  $R_C$  into  $R_{ci}$  and  $R_{junn}$ .<sup>[29–31]</sup>  $R_{ci}$  is the resistance component under the electrode that consists of  $\rho_c$  and  $R_{sk}$ . Here, when using our FLP-free devices, the gate-

tunable  $R_{junn}$  is mostly attributable to the difference in doping concentration between MoS<sub>2</sub> under the contact and at the channel area that originates from heavy n-type doping in MoS<sub>2</sub> by semimetal Sb, forming a gate-tunable n<sup>+</sup>-n junction. Figure 1b represents a schematic of a DG MoS<sub>2</sub> FET showing the impact of  $V_{TG}$  and  $V_{BG}$  on contact resistance components of the device. As Ber et al. reported,  $R_{ci}$  is weakly dependent on  $V_{BG}$  due to FLP and high doping concentration under the contact.<sup>[29]</sup> Moreover,  $R_{ci}$  is supposed to be independent of  $V_{TG}$ , as the electric field induced by  $V_{TG}$  ( $E_{TG}$  as indicated in the diagram) is screened by the covered metal electrodes. In contrast,  $R_{junn}$  is found to be  $V_{BG}$  tunable due to the modulation of lateral junction potential.<sup>[29–31]</sup> Furthermore,  $R_{junn}$  is supposed to be strongly modulated by  $V_{TG}$  unlike  $R_{ci}$  as it is not covered by the metal electrode.<sup>[29–31]</sup> Thus, we believe that overall  $R_C$  could be affected by applying  $V_{BG}$  and  $V_{TG}$  simultaneously in the DG structure considering such strong modulation of  $R_{junn}$ .

To investigate the impact of  $V_{TG}$  on  $R_C$ , we fabricated DG MoS<sub>2</sub> FETs with Sb (and DG MoS<sub>2</sub> FETs with Ti as a reference) electrodes on a global bottom-gate (BG) silicon substrate capped with 285 nm SiO<sub>2</sub> (To ensure the screening effect of metal electrode against  $V_{TG}$ , total thickness of  $\approx 25$  nm is used).<sup>[33]</sup> The TG of the device is formed by an exfoliated hBN flake ( $\approx 50$  nm) with a TG electrode of Ti/Au (5/70 nm). The detailed fabrication process is described in the Experimental Section. The Raman spectra and atomic force microscopic (AFM) images of MoS<sub>2</sub> and hBN are shown in Figure S1 (Supporting Information). The dry-transferred hBN possibly results in the formation of air gap at the metal-MoS<sub>2</sub> junction where the top hBN is not fully contacted with MoS<sub>2</sub> channel. However, if we consider the air gap as a dielectric layer with a dielectric constant of 1, MoS<sub>2</sub> area at the gap is still electrostatically tunable by  $V_{TG}$ . In this sense, Zhang et al. have reported that 2D semiconductors can be electrostatically doped by applying gate-voltages despite the existence of air gap at the metal-2D semiconductor junction.<sup>[33]</sup> Therefore, although the existence of the air gap at metal-MoS<sub>2</sub> junction may affect the top-gate performance, the electrostatic modulation of  $R_C$  and  $R_{junn}$  by  $V_{TG}$  is still possible.

**Figure 2a** illustrates the final structure of the DG MoS<sub>2</sub> FET. The transfer characteristic of the DG FET with Sb contacts is depicted in Figure 2b. The device with  $L_{CH} = 11.5$   $\mu\text{m}$  achieves  $I_{ON}$  of  $\approx 8$   $\mu\text{A } \mu\text{m}^{-1}$  at  $V_{DS} = 1$  V with a good  $I_{ON}/I_{OFF}$  ratio of  $\approx 10^7$  without  $V_{TG}$ . The Ohmic behavior of Sb contact is evidenced by the linear output characteristic, as represented in Figure 2c. It is

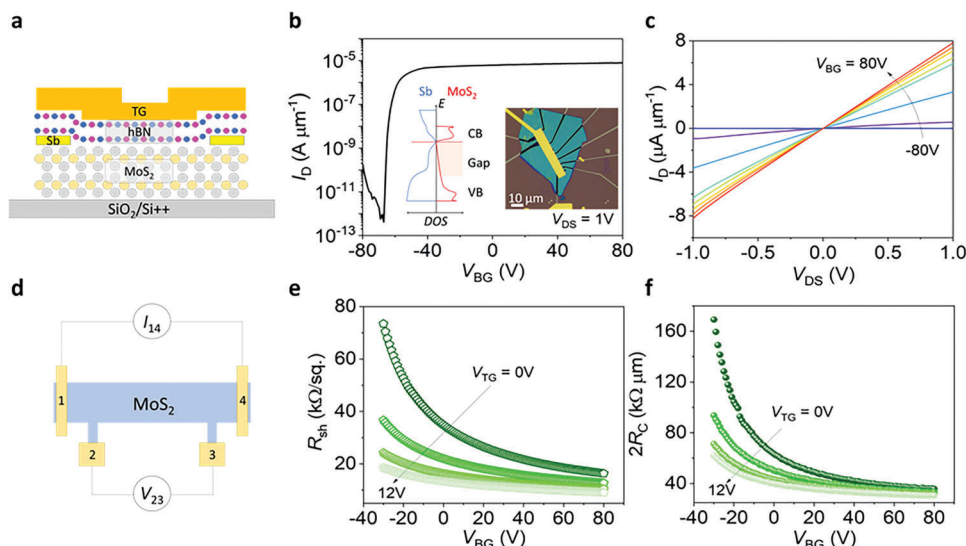


**Figure 2.** a) Schematic of a Sb-contacted DG MoS<sub>2</sub> FET. b) Transfer characteristics of the FET with  $V_{DS} = 1$  V and  $V_{TG} = 0$  V. The insets show an optical image of the device and a band structure showing the DOS of Sb and MoS<sub>2</sub>. c) Output characteristic of the FET by varying  $V_{BG} = -80$  to 80 V ( $V_{TG} = 0$  V). d) Schematic of a 4PP measurement configuration of the FET. e)  $R_{sh}$  and f)  $2R_C$  as a function of  $V_{BG}$  at different  $V_{TG}$  obtained from the FET.

noted that the linear behavior is also obtained without gating the contact area by sweeping  $V_{TG}$  from  $-12$  to  $12$  V at  $V_{BG} = 0$  V (Figure S2, Supporting Information), which shows the superiority of Sb semimetal over normal metals. The mobilities and hysteresis behavior of Sb-contacted DG MoS<sub>2</sub> FETs extracted from the transfer curves with  $V_{TG}$  and  $V_{BG}$  are shown in Figures S3 and S4 (Supporting Information). As a reference, the transfer and output characteristics of Ti-contacted DG MoS<sub>2</sub> FET are shown in Figure S5 (Supporting Information). Unlike Sb contacts, asymmetric output characteristics are observed with both  $V_{TG}$  and  $V_{BG}$  in Ti-contacted device. We further demonstrate the distinctive  $V_{TG}$ -dependent transfer characteristics of the Sb-contacted device compared to the Ti-contacted device as shown in Figure S6 (Supporting Information). Both devices show a similar improvement in on-state current when  $V_{TG}$  increases; however, the threshold voltage ( $V_{th}$ ) of the Sb-contacted device is strongly shifted to negative  $V_{TG}$ , while the Ti-contacted device revealed a slight  $V_{th}$  shift. The origin of this phenomenon can be explained by the different  $V_{TG}$ -dependent  $R_C$  between both devices as discussed in Figure 3.

To evaluate the FLP behavior of the devices, we further conducted temperature-dependent measurements of the transfer characteristics to extract Schottky barrier height (SBH), as depicted in Figure S7 (Supporting Information). The Sb-contacted device shows a negligible SBH ( $\approx 0$  meV), while the Ti-contacted device shows a relatively high SBH ( $\approx 200$  meV) despite the fact that both the metals have similar work functions (4.4 eV for Sb and 4.33 eV for Ti).<sup>[8,34]</sup> The FLP behavior of both devices can be understood by band alignment, as depicted in Figure S7d,e (Supporting Information). The negligible SBH of the Sb-contacted device is consistent with intrinsic band alignment showing FLP-free contact for the 2D MoS<sub>2</sub> FET. This FLP-free behavior is consistent with the DFT calculation performed by Chou et al., which shows suppressed MIGS (inset of Figure 2b).<sup>[9]</sup> Ti is supposed to have Ohmic contact with 2D MoS<sub>2</sub> ( $\approx 0$  meV) according to the iso-

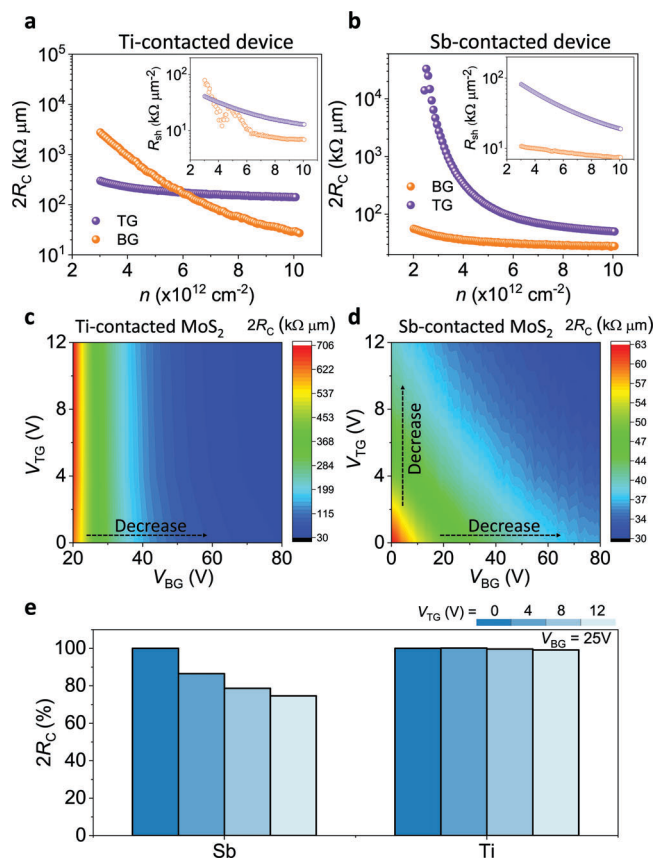


**Figure 3.**  $2R_C$  of a) Ti- and b) Sb-contacted devices measured by 4PP measurements with separate TG and BG biases. The inset shows  $R_{sh}$  as a function of carrier densities.  $2R_C$  map as a function of  $V_{TG}$  and  $V_{BG}$  for c) Ti- and d) Sb-contacted DG MoS<sub>2</sub> FETs. e) Modulated percentages of  $2R_C$  as a function of  $V_{TG}$  at a fixed  $V_{BG} = 25$  V.

lated band structure, but the actual SBH is  $\approx 200$  meV, implying a strong FLP.

Figure 2d illustrates the device configuration used in the 4PP measurements to extract the  $R_C$  of the DG MoS<sub>2</sub> devices. A fixed current ( $I_{14} = 0.33 \mu\text{A}\cdot\mu\text{m}^{-1}$ ) is applied between electrodes 1 and 4, and the voltage is probed at each electrode. By measuring the voltage drop between electrodes 2 and 3 ( $\Delta V_{23}$ ), sheet resistance ( $R_{sh}$ ) can be calculated by:

$$R_{sh} = \frac{\Delta V_{23}}{I_{14} \times L_{23}} \quad (1)$$

Moreover,  $R_C$  can be calculated by:

$$2R_C = \frac{\Delta V_{14}}{I_{14}} - \frac{\Delta V_{23} \times L_{14}}{I_{14} \times L_{23}} \quad (2)$$

where  $L_{14} = 11.5 \mu\text{m}$  and  $L_{23} = 5.8 \mu\text{m}$  are the distances between electrodes 1–4 and 2–3, respectively. Figure 2e exhibits  $R_{sh}$  as a function of  $V_{BG}$  that shows strong gate-tunability with  $V_{BG}$  and  $V_{TG}$ , since  $R_{ch}$  is gate-tunable, as depicted in Figure 1b. We observed a noticeable reduction in  $R_{sh}$  from 16 to 9 k $\Omega$  per square when  $V_{TG}$  increases from 0 to 12 V, which is a typical behavior for n-type semiconductors. This observation is consistent with previous results for DG 2D FETs.<sup>[17,19,20]</sup> Figure 2f presents the  $R_C$  as a function of  $V_{TG}$  derived from Equation (2). Interestingly, we noticed a considerable improvement in  $R_C$  (63 to 40 k $\Omega\mu\text{m}$  at  $V_{BG} = 0$  V) with the increase in  $V_{TG}$  from 0 to 12 V. This behavior can be reproduced in other separately prepared devices as shown in Figure S8 and S9. In all devices,  $R_C$  of Sb-contacted device strongly depends on  $V_{TG}$ . The strong  $V_{TG}$ -tunability of overall  $R_C$  in Sb-contacted DG MoS<sub>2</sub> FETs is in contrast to the results obtained from the previous studies with normal metal contacts.<sup>[19,20]</sup> The almost unchanged  $R_C$  regardless of  $V_{TG}$  in these studies can be attributed to the screening effect of  $E_{TG}$  by top-contact metals and strong FLP.<sup>[19,20]</sup>

For a comparison, we also performed the same 4PP measurement with Ti-contacted DG MoS<sub>2</sub> FETs. The  $R_{sh}$  and  $R_C$  values measured at different  $V_{TG}$  and  $V_{BG}$  of the devices are presented in Figure S10 (Supporting Information). The  $2R_C$  and  $R_{sh}$  measured with separate  $V_{TG}$  and  $V_{BG}$  for both the Sb- and Ti-contacted devices are represented in Figure 3a,b. For a fair comparison, we plotted the  $R_{sh}$  and  $R_C$  as a function of carrier concentration, which is extracted by the equation,  $n = q^{-1} C_{TG}(V_{TG} - V_{th})$ , where  $q$  is the electron charge and  $C_{TG}$  is the TG capacitance ( $= 1.23 \times 10^{-7} \text{ F cm}^{-2}$  for a 50 nm thick top hBN gate dielectric). The  $R_{sh}$  of both devices demonstrate a similar trend and values; however,  $R_C$  tunability is clearly different. The  $R_C$  of the Sb-contacted device is strongly  $V_{TG}$  tunable, while a weak  $V_{TG}$ -dependent  $R_C$  is obtained with the Ti-contacted device. Thus, we think that the difference in transfer characteristics of both the devices (different  $V_{th}$  shift with  $V_{TG}$  in Figure S6, Supporting Information) is mostly originated from the strong  $V_{TG}$ -dependent  $R_C$  of the Sb-contacted device compared to the weak  $V_{TG}$ -dependent  $R_C$  of the Ti-based device, as shown in Figure 3a,b.

Based on Figure 2f and Figure S10b (Supporting Information), we reproduced  $R_C$  map to visualize the different trends in  $R_C$  between Ti and Sb contacts depending on  $V_{TG}$  and  $V_{BG}$ , as depicted in Figure 3c,d. For the Ti-contacted device,  $R_C$  is modu-

lated by  $V_{BG}$ , while it remains unchanged by  $V_{TG}$ , as shown in the color gradient of the map, indicating that  $R_C$  is dominated by  $V_{BG}$  (Figure 3a). This phenomenon has also been observed in previous studies with the same device architecture and normal metals.<sup>[19,20]</sup> By contrast, a distinctive behavior is observed with the Sb-contacted device;  $R_C$  varies largely by both  $V_{BG}$  and  $V_{TG}$ , as can be seen from the continuous variation of color gradient in Figure 3d. Figure 3e presents such  $2R_C$  change in percentage as a function of  $V_{TG}$ , showing a roughly 30% improvement when  $V_{TG}$  increases from 0 to 12 V with Sb contacts. However, Ti contact reduces  $2R_C$  by merely  $\approx 1\%$  with the same  $V_{TG}$  condition.

To elucidate the origin of the anomalous behavior of Sb-contacted device, we utilized the method proposed by Ber et al.<sup>[29]</sup> to extract  $R_{jun}$  and  $R_{ci}$  based on the  $2R_C$  value obtained by 4PP measurements, thereby identifying predominant resistance components in  $R_C$ . Figure 4a illustrates an equivalent circuit and a corresponding band structure, including  $R_{jun}$  and  $R_{ci}$  at the MS interface.<sup>[29,30]</sup> The total contact resistance is expressed by:

$$2R_C = 2R_{ci} + R_{jun} \quad (3)$$

Here,  $R_{ci}$  is multiplied by 2 as the current passes through the source and drain electrodes.  $R_{jun}$  is found at the contact where the current is injected, thus, it is considered to have appeared only once in the above expression.<sup>[29]</sup> Next, the resistance between the current injecting electrode and the nearest voltage probing electrode ( $R_{12}$ ) is expressed as:

$$R_{12} = \frac{\Delta V_{12}}{I_{14}} = R_{ci} + R_{jun} + R_{sh}L_{12} \quad (4)$$

where  $L_{12}$  ( $= 3.2 \mu\text{m}$ ) is the distance between electrodes 1 and 2. Based on Equations (3) and (4), we extracted  $R_{jun}$  and  $R_{ci}$  using the value of  $2R_C$  obtained through 4PP measurements. Figure 4b shows the calculated  $R_{jun}$  and  $R_{ci}$  values of the Sb-contacted device at  $V_{BG} = -30$  to 80 V and  $V_{TG} = 0$  V. It should be noted that  $R_{jun}$  is strongly dependent on  $V_{BG}$ , unlike  $R_{ci}$ .  $R_{jun}$  can mainly originate from the strong electron doping effect of semimetal to MoS<sub>2</sub> underneath the contact, thus resulting in the formation of  $n^+ - n$  junction, where an n-type region is located at the channel side.<sup>[8,29]</sup> The contribution of SBH can be negligible in  $R_{jun}$  due to the FLP-free nature of semimetal contacts, as shown in Figure S7 (Supporting Information). Therefore, the potential barrier at the junction can be reduced when  $V_{BG}$  increases because the n-region becomes a highly doped  $n^+$ -state as a result of electrostatic doping due to weak FLP. However, the  $n^+$ -region underneath the semimetal is not significantly affected by  $V_{BG}$  due to its high electron concentration.<sup>[6,35,36]</sup>

Figure 4c shows  $R_{jun}$  of the Sb-contacted DG device as a function of  $V_{BG}$  with different  $V_{TG}$ . Interestingly,  $R_{jun}$  is highly modulated by  $V_{TG}$ , confirming that  $E_{TG}$  can modulate  $R_C$ . At high  $V_{TG} = 12$  V,  $R_{jun}$  becomes independent of  $V_{BG}$ . This validates the fact that the electrostatic doping effect of  $E_{TG}$  significantly suppresses the potential barrier, equalizing the electron concentration of both MoS<sub>2</sub> under the metal contact and at the channel area. In contrast,  $R_{ci}$  is very weakly dependent on  $V_{TG}$  as shown in Figure 4d, which can be understood as the metal screening effect. Thus, the improvement in  $R_C$  by  $V_{TG}$ , as shown in Figure 2f and 3b, is mostly attributed to the reduced  $R_{jun}$ .

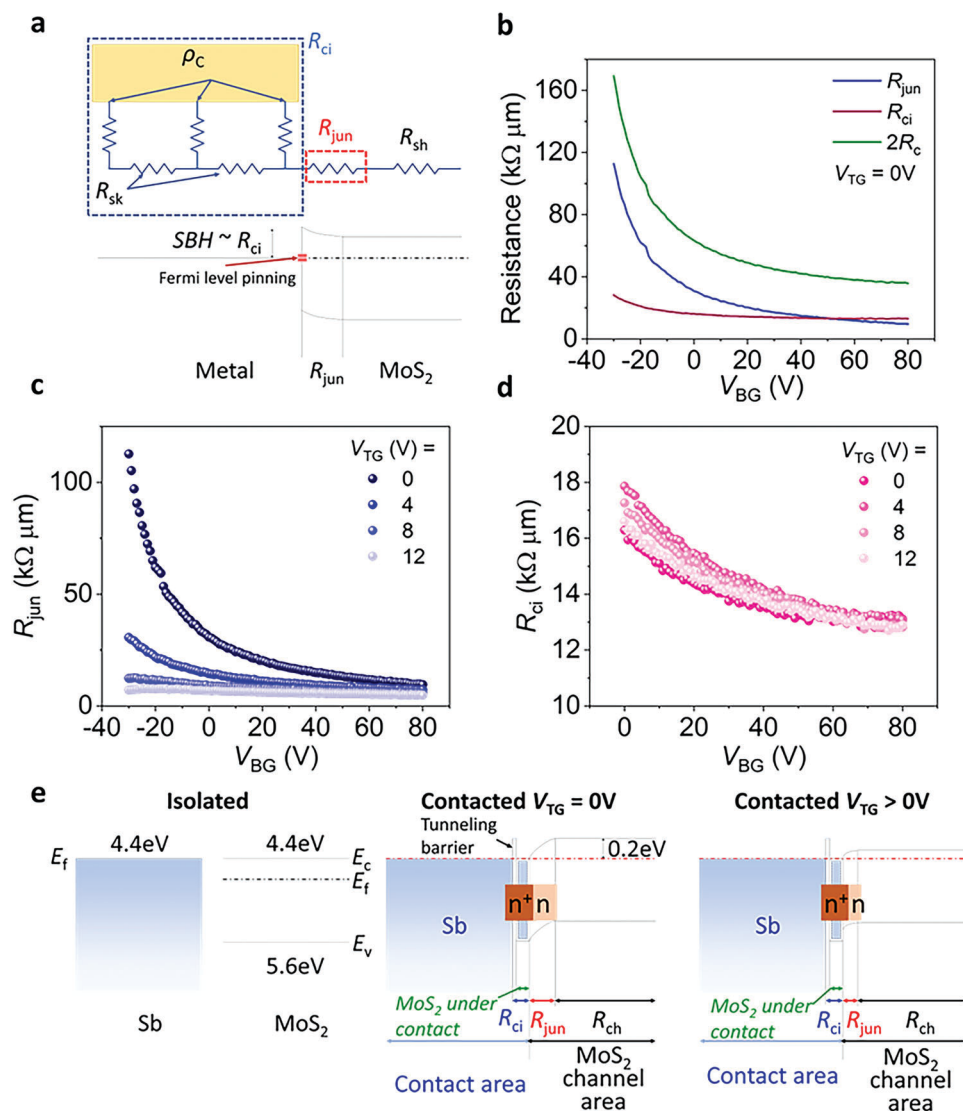


**Figure 4.** a) An equivalent circuit with resistance components at the MS contact and a corresponding band diagram illustrating FLP. b)  $R_{ci}$ ,  $R_{jun}$ , and  $2R_c$  as a function of  $V_{BG}$  at  $V_{TG} = 0$  V, and c)  $R_{jun}$  and d)  $R_{ci}$  as a function of  $V_{BG}$  and  $V_{TG}$  for the Sb-contacted DG MoS<sub>2</sub> FET. e) Band diagrams for Sb-contacted MoS<sub>2</sub> illustrating how  $R_{jun}$  is modulated by  $V_{TG}$ .

The band diagram in Figure 4e describes the mechanism by which  $V_{TG}$  adjusts  $R_{jun}$ . At  $V_{TG} = 0$  V, the potential barrier is formed by band alignment between MoS<sub>2</sub> and Sb based on their work functions. As a result, MoS<sub>2</sub> underneath Sb contact is strongly n-type doped, forming a n<sup>+</sup>-n lateral junction with MoS<sub>2</sub> at the channel area. Therefore, the n<sup>+</sup>-n lateral junction dominantly contributes to  $R_{jun}$ . When  $V_{TG}$  increases, the Fermi level of MoS<sub>2</sub> at the channel area is expected to move upward, leading to a reduced potential barrier. Moreover, the depletion width in n<sup>+</sup>-n lateral junction decreases by equalizing the doping concentration between MoS<sub>2</sub> underneath the contact and at the channel area. This reduction in potential barrier and depletion width at high  $V_{TG}$  contributes to the decreased  $R_{jun}$ .

For the Ti-contacted device, the extracted  $R_{jun}$  and  $R_{ci}$  are presented in Figure S10c,d (Supporting Information). Unlike the Sb-contacted device,  $R_{jun}$  is weakly dependent on  $V_{TG}$ , presum-

ably due to strong FLP. Since the Fermi level of MoS<sub>2</sub> is strongly pinned at the MIGS or defect states, it barely shifts by  $V_{TG}$ , particularly at the MS interface. Since  $R_{ci}$  is also independent of  $V_{TG}$ ,  $R_c$  for the Ti-contacted device appears to be overall unchanged by  $V_{TG}$ . This interpretation is further supported by a recent work on DFT calculation, which shows tunable band alignment of MS contact with Sb contacts due to their lack of MIGS, while unnoticeable tunability is observed with normal metals.<sup>[13]</sup> Consequently, our work provides a distinctive advantage of semimetal-contacted DG device in terms of its ability to modulate  $R_c$  with  $V_{TG}$ .

Last, we verify our experimental results and mechanism by performing TCAD simulations. Figure 5a shows a device structure of Sb-contacted DG device used for our simulations (detailed information and parameters are described in the Experimental Section and Table S1, Supporting Information). The simulation

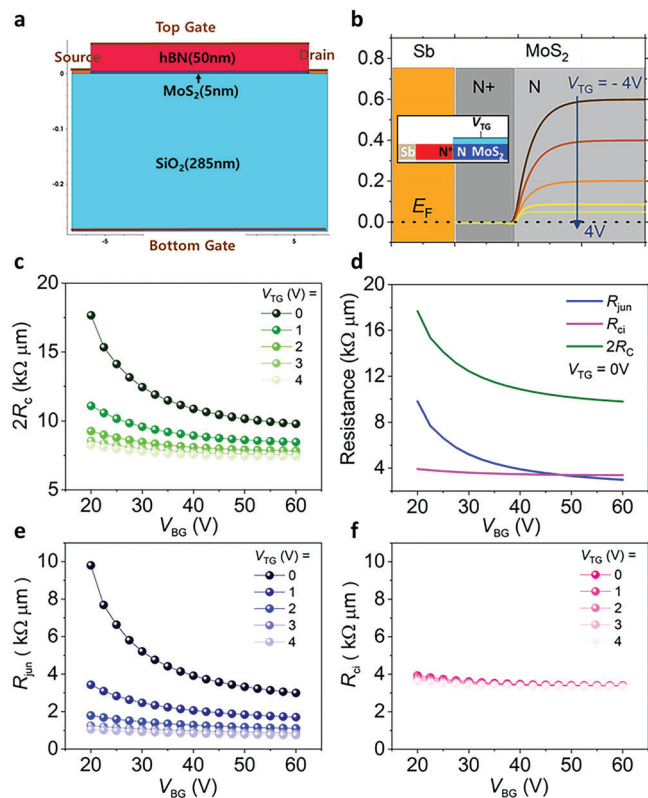


**Figure 5.** a) Device structure for TCAD simulations. b) Band alignment between Sb and MoS<sub>2</sub> with varied  $V_{TG}$ . c) Simulated  $2R_C$  of Sb-contacted DG device as a function of  $V_{TG}$  and  $V_{BG}$ . d) Simulated  $R_{ci}$ ,  $R_{jun}$ , and  $2R_C$  as a function of  $V_{BG}$  at  $V_{TG} = 0$  V. Simulated e)  $R_{jun}$  and f)  $R_{ci}$  as a function of  $V_{BG}$  and  $V_{TG}$ .

assumes that the SBH of Sb-contacted DG device to be zero due to its FLP-free nature, as confirmed by our SBH measurement in Figure S7 (Supporting Information). Furthermore, the n<sup>+</sup>-n junction is considered at the MS junction as Sb semimetal can induce heavy n-type doping to MoS<sub>2</sub>. As shown in Figure 5b, the potential barrier of Sb-contacted DG device significantly decreases as  $V_{TG}$  increases, which is consistent with our above postulation on strong modulation of  $R_C$  and  $R_{jun}$  by  $V_{TG}$ . The strong modulation can also be seen in the simulation results from Figure 5c,e. Moreover, the simulated  $R_{ci}$  remains almost unchanged as depicted in Figure 5f due to the heavy n-doping effect of Sb, which is also in good agreement with our experimental results. For the Ti-contacted device, however, the simulated  $2R_C$  remains constant with varied  $V_{TG}$  attributed to weak tunability of  $R_{jun}$  and  $R_{ci}$  (Figure S11), due to strong FLP. We performed further TCAD simulation to investigate how the transfer length ( $L_T$ ) and junction length ( $L_{jun}$ ) affect resistance components of the devices, as presented in Figures S12 and S13 (Supporting Information). When  $L_T$  increases up to 50 nm,  $R_{jun}$  of the device slightly decreases, while  $R_{jun}$  remains almost unchanged when  $L_T$  is greater than 50 nm. Thus, we believe that a further increase in  $L_T$  does not modulate the  $R_{jun}$  significantly, as depicted in Figure S12. Meanwhile, we found that increased  $L_{jun}$  results in a significant increase in  $R_{jun}$ , while  $R_{ci}$  remains almost constant regardless of  $L_{jun}$ , as shown in Figure S13 (Supporting Information). Here,  $L_{jun}$

is much more dominant in modulating  $R_{jun}$  than  $L_T$  when comparing Figures S12 and S13 (Supporting Information), suggesting  $L_{jun}$  is a key parameter for understanding the contact properties of 2D devices. Consequently, the TCAD simulations further demonstrate the origin of distinctive gate-dependent contact parameters between Ti and Sb contacts.

### 3. Conclusion

In conclusion, we conducted a comprehensive study on the electrical properties of MoS<sub>2</sub> devices contacted with semimetal (Sb) and normal metal (Ti) electrodes as a function of  $V_{TG}$  and  $V_{BG}$ . The Sb-contacted FETs revealed not only the negligible Schottky barrier but also a new insight on the role of DG structure to modulate  $R_C$ , which has not been reported in previous reports. The DG structure combining with semimetal contacts revealed the strong dependence of  $R_C$  on  $V_{TG}$ -when compared to the devices with normal metallic contacts. We utilized a new model that considers  $R_{jun}$  component to the total  $R_C$ , which shows that the weak FLP nature of semimetals modulates  $R_{jun}$  and is responsible for the significantly modulated  $R_C$  by  $V_{TG}$ . In contrast, the strong FLP in Ti-contacted devices limits the top gate-tunability of  $R_{jun}$ , resulting in unchanged  $R_C$ . TCAD simulations provided further confirmation of the contribution of  $V_{TG}$  to  $R_{jun}$  and the overall  $R_C$  improvement of Sb-contacted MoS<sub>2</sub> devices. The FLP-free Sb contact in DG device architecture has a significant advantage in the effective gate control of  $R_C$ , which can help achieve high-performance 2D FETs.

### 4. Experimental Section

**Device Fabrication Process:** The 2D materials (hBN and MoS<sub>2</sub>) were mechanically exfoliated using the scotch-tape method before being transferred onto a degenerately p-doped Si wafer covered by 285 nm of thermally grown SiO<sub>2</sub>, which is served as a global gate dielectric. The thickness of MoS<sub>2</sub> flakes (<5 nm) was identified by optical contrast. PMMA A6 resist was spin-coated to form a mask, followed by the electron beam lithography (EBL) process for device patterning. Subsequently, Sb/Au (Ti/Au) metal contacts with a thickness of 5/20 (5/20) nm were directly deposited with an e-beam evaporator at a vacuum pressure of  $5 \times 10^{-7}$  Torr. The top dielectric was formed by covering the whole structure with hBN flake ( $\approx 50$  nm) via a dry pick-up and transfer process. The top gate electrode was formed through EBL patterning followed by a Ti/Au (5/70) deposition process.

**Device Characterization:** All electrical measurements were performed using a semiconductor parameter analyzer (Agilent 4155C) connected to a vacuum probe station with pressure maintained at 20 mTorr.

**TCAD Simulations:** Device analysis was performed through Synopsys Sentaurus (Synopsys Inc., Mountain View, CA, USA), a 3D technology computer-aided design (TCAD) software package. To describe the energy band characteristics of MoS<sub>2</sub> as a channel, the room temperature effective density-of-states  $N_C$  (300 K) and  $N_V$  (300 K) of  $7.947 \times 10^{19} \text{ cm}^{-3}$  and  $9.674 \times 10^{19} \text{ cm}^{-3}$ , respectively, the bandgap of 1.2 eV, and dielectric constants of  $\epsilon_{\perp} = 6.4$  and  $\epsilon_{\parallel} = 15.1$  were used.<sup>[37]</sup> The work function of 4.4 eV was used for both Sb and Ti metals, and SBH = 0 eV was realized at the interface between MoS<sub>2</sub> and Sb due to its FLP-free nature. In addition, the Sze model among the FLP models was used to describe the interface characteristics of MoS<sub>2</sub> and Ti. The density of interface states per unit energy ( $N_i$ ) of  $8.5 \times 10^{12} \text{ cm}^{-2} \text{ eV}^{-1}$ , their extent into the semiconductor ( $d$ ) of  $2 \times 10^{-7} \text{ cm}$ , and charge neutrality level ( $E_{CNL}$ ) of 5.00 eV were used to implement Schottky barrier height of 0.2 eV.

## Supporting Information

Supporting Information is available from the Wiley Online Library or from the author.

## Acknowledgements

This work was supported by the Global Research Laboratory (GRL) Program (2016K1A1A2912707), and the Basic Science Research Program (2021R1A2C2010869, 2022R1C1C2005607), funded by the National Research Foundation of Korea (NRF). It was also partially supported by the Ministry of Trade, Industry and Energy (20022369).

## Conflict of Interest

The authors declare no conflict of interest.

## Data Availability Statement

The data that support the findings of this study are available from the corresponding author upon reasonable request.

## Keywords

2D semiconductors, contact resistance, dual-gate, Fermi level pinning-free, four-point-probe measurements, junction resistance, semimetal

Received: March 25, 2023

Revised: April 23, 2023

Published online:

- [1] L. Wang, P. Y. Huang, Q. Gao, Y. Gao, H. Tran, T. Taniguchi, K. Watanabe, L. M. Campos, D. A. Muller, J. Guo, P. Kim, J. Hone, K. L. Shepard, C. R. Dean, *Science* **2013**, *342*, 614.
- [2] T. D. Ngo, Z. Yang, M. Lee, F. Ali, I. Moon, D. G. Kim, T. Taniguchi, K. Watanabe, K.-Y. Lee, W. J. Yoo, *Adv. Electron. Mater.* **2021**, *7*, 2001212.
- [3] Y. Liu, J. Guo, E. Zhu, L. Liao, S.-J. Lee, M. Ding, I. Shakir, V. Gambin, Y. Huang, X. Duan, *Nature* **2018**, *557*, 696.
- [4] Y. Jung, M. S. Choi, A. Nipane, A. Borah, B. Kim, A. Zangiabadi, T. Taniguchi, K. Watanabe, W. J. Yoo, J. Hone, J. T. Teherani, *Nat. Electron.* **2019**, *2*, 187.
- [5] Z. Yang, C. Kim, K. Y. Lee, M. Lee, S. Appalakondaiah, C.-H. Ra, K. Watanabe, T. Taniguchi, K. Cho, E. Hwang, J. Hone, W. J. Yoo, *Adv. Mater.* **2019**, *31*, 1808231.
- [6] T. D. Ngo, M. S. Choi, M. Lee, F. Ali, Y. Hassan, N. Ali, S. Liu, C. Lee, J. Hone, W. J. Yoo, *Adv. Sci.* **2022**, *9*, 2202465.
- [7] S. Cho, S. Kim, J. H. Kim, J. Zhao, J. Seok, D. H. Keum, J. Baik, D.-H. Choe, K. J. Chang, K. Suenaga, S. W. Kim, Y. H. Lee, H. Yang, *Science* **2015**, *349*, 625.
- [8] P.-C. Shen, C. Su, Y. Lin, A.-S. Chou, C.-C. Cheng, J.-H. Park, M.-H. Chiu, A.-Y. Lu, H.-L. Tang, M. M. Tavakoli, G. Pitner, X. Ji, Z. Cai, N. Mao, J. Wang, V. Tung, J. Li, J. Bokor, A. Zettl, C.-I. Wu, T. Palacios, L.-J. Li, J. Kong, *Nature* **2021**, *593*, 211.
- [9] A.-S. Chou, T. Wu, C.-C. Cheng, S.-S. Zhan, I.-C. Ni, S.-Y. Wang, Y.-C. Chang, S.-L. Liew, E. Chen, W.-H. Chang, C.-I. Wu, J. Cai, H.-S. P. Wong, H. Wang, in Proc. 2021 IEEE Int. Electron Devices Meeting (IEDM), IEEE, San Francisco, CA, USA **2021**, pp. 7.2.1-7.2.4.
- [10] K. P. O'Brien, C. J. Dorow, A. Penumatcha, K. Maxey, S. Lee, C. H. Naylor, A. Hsiao, B. Holybee, C. Rogan, D. Adams, T. Tronic, S. Ma, A. Oni, A. Sen Gupta, R. Bristol, S. Clendenning, M. Metz, U. Avci, in Proc. 2021 IEEE Int. Electron Devices Meeting (IEDM), IEEE, San Francisco, CA, USA **2021**, pp. 7.1.1-7.1.4.
- [11] Y. Wan, E. Li, Z. Yu, J.-K. Huang, M.-Y. Li, A.-S. Chou, Y.-T. Lee, C.-J. Lee, H.-C. Hsu, Q. Zhan, A. Aljarb, J.-H. Fu, S.-P. Chiu, X. Wang, J.-J. Lin, Y.-P. Chiu, W.-H. Chang, H. Wang, Y. Shi, N. Lin, Y. Cheng, V. Tung, L.-J. Li, *Nat. Commun.* **2022**, *13*, 4149.
- [12] W. Li, D. Fan, L. Shao, F. Huang, L. Liang, T. Li, Y. Xu, X. Tu, P. Wang, Z. Yu, Y. Shi, H. Qiu, X. Wang, in Proc. 2021 IEEE Int. Electron Devices Meeting (IEDM), IEEE, San Francisco, CA, USA **2021**, pp. 37.3.1-37.3.4.
- [13] Y. Cho, G. R. Schleder, D. T. Larson, E. Brutschea, K.-E. Byun, H. Park, P. Kim, E. Kaxiras, *Nano Lett.* **2022**, *23*, 9700.
- [14] J. Lin, S. J. Koester, *IEEE Electron Device Lett.* **2022**, *43*, 639.
- [15] A. Kumar, K. Schauble, K. M. Neilson, A. Tang, P. Ramesh, H.-S. P. Wong, E. Pop, K. Saraswat, in Proc. 2021 IEEE Int. Electron Devices Meeting (IEDM), IEEE, San Francisco, CA, USA **2021**, pp. 7.3.1-7.3.4.
- [16] Y. Shen, Z. Dong, Y. Sun, H. Guo, F. Wu, X. Li, J. Tang, J. Liu, X. Wu, H. Tian, T.-L. Ren, *Adv. Mater.* **2022**, 2201916.
- [17] H. C. P. Movva, A. Rai, S. Kang, K. Kim, B. Fallahzad, T. Taniguchi, K. Watanabe, E. Tutuc, S. K. Banerjee, *ACS Nano* **2015**, *9*, 10402.
- [18] T. Wei, Z. Han, X. Zhong, Q. Xiao, T. Liu, D. Xiang, *iScience* **2022**, *10*, 105160.
- [19] M. A. Rodder, A. Dodapalapur, *IEEE Trans. Electron Devices* **2019**, *66*, 4468.
- [20] Z. Sun, C.-S. Pang, P. Wu, T. Y. T. Hung, M.-Y. Li, S. L. Liew, C.-C. Cheng, H. Wang, H.-S. P. Wong, L.-J. Li, I. Radu, Z. Chen, J. Appenzeller, *ACS Nano* **2022**, *16*, 14942.
- [21] J. Tang, Q. Wang, Z. Wei, C. Shen, X. Lu, S. Wang, Y. Zhao, J. Liu, N. Li, Y. Chu, J. Tian, F. Wu, W. Yang, C. He, R. Yang, D. Shi, K. Watanabe, T. Taniguchi, G. Zhang, *Adv. Electron. Mater.* **2020**, *6*, 2000550.
- [22] X. Huang, C. Liu, S. Zeng, Z. Tang, S. Wang, X. Chen, D. W. Zhang, P. Zhou, *Adv. Mater.* **2021**, *33*, 2102201.
- [23] X. Huang, C. Liu, Z. Tang, S. Zeng, L. Liu, X. Hou, H. Chen, J. Li, Y.-G. Jiang, D. W. Zhang, P. Zhou, in Proc. 2021 IEEE Int. Electron Devices Meeting (IEDM), IEEE, San Francisco, CA, USA **2020**, pp. 12.1.1-12.1.4.
- [24] M. Liu, J. Niu, G. Yang, K. Chen, W. Lu, F. Liao, C. Lu, N. Lu, L. Li, *Adv. Electron. Mater.* **2022**, *9*, 2200722.
- [25] C. J. Dorow, A. Penumatcha, A. Kitamura, C. Rogan, K. P. O'Brien, S. Lee, R. Ramamurthy, C.-Y. Cheng, K. Maxey, T. Zhong, T. Tronic, B. Holybee, J. Richards, A. Oni, C.-C. Lin, C. H. Naylor, N. Arefin, M. Metz, R. Bristol, S. B. Clendenning, U. Avci, in Proc. 2022 IEEE Int. Electron Devices Meeting (IEDM), IEEE, San Francisco, CA, USA **2022**, pp. 7.5.1-7.5.4.
- [26] C. Kim, I. Moon, D. Lee, M. S. Choi, F. Ahmed, S. Nam, Y. Cho, H. J. Shin, S. Park, W. J. Yoo, *ACS Nano* **2017**, *11*, 1588.
- [27] T. D. Ngo, M. Lee, Z. Yang, F. Ali, I. Moon, W. J. Yoo, *Adv. Electron. Mater.* **2020**, *6*, 2000616.
- [28] A. Allain, J. Kang, K. Banerjee, A. Kis, *Nat. Mater.* **2015**, *14*, 1195.
- [29] a) E. Ber, R. W. Grady, E. Pop, E. Yalon, (Preprint) arXiv:2110.02563, v1, submitted: Oct **2021**; b) E. Ber, R. W. Grady, E. Pop, E. Yalon, *Adv. Electron. Mater.* **2023**, <https://doi.org/10.1002/aelm.202201342>.
- [30] S. Venica, F. Driussi, A. Gahoi, P. Palestri, M. C. Lemme, L. Selmi, *IEEE Trans. Electron Devices* **2018**, *65*, 1589.
- [31] A. Gahoi, S. Kataria, F. Driussi, S. Venica, H. Pandey, D. Esseni, L. Selmi, M. C. Lemme, *Adv. Electron. Mater.* **2020**, *6*, 2000386.
- [32] L. Kong, X. Zhang, Q. Tao, M. Zhang, W. Dang, Z. Li, L. Feng, L. Liao, X. Duan, Y. Liu, *Nat. Commun.* **2020**, *11*, 1866.
- [33] G. Zhang, G. Lu, X. Li, Z. Mei, L. Liang, S. Fan, Q. Li, Y. Wei, *ACS Nano* **2023**, *17*, 4564.
- [34] D. R. Lide, *CRC Handbook of Chemistry and Physics*, CRC Press, Boca Raton, FL **2001**.
- [35] Y. Yang, N. Huo, J. Li, *J. Mater. Chem. C* **2017**, *5*, 7051.
- [36] P. Wen, L. Zhang, W. Gao, Q. Yue, H. Wang, Y. Huang, J. Wu, H. Yu, H. Chen, N. Huo, J. Li, *Adv. Electron. Mater.* **2022**, *8*, 2101144.
- [37] A. Laturia, M. L. Van de Put, W. G. Vandenberghe, *npj 2D Mater. Appl.* **2018**, *2*, 6.